Spatially Resolved Observation of Static Magnetic Flux States in $YBa_2Cu_3O_{7-\delta}$ Grain Boundary Josephson Junctions

G. M. Fischer,* B. Mayer, R. Gross, T. Nissel, K.-D. Husemann, R. P. Huebener, T. Freltoft, Y. Shen, P. Vase

With low-temperature scanning electron microscopy, the magnetic flux states in high critical temperature Josephson junctions have been imaged. The experiments were performed with $YBa_2Cu_3O_{7-\delta}$ thin-film grain boundary Josephson junctions fabricated on [001] tilt $SrTiO_3$ bicrystals. For applied magnetic fields parallel to the grain boundary plane, which correspond to local maxima of the magnetic field dependence of the critical current, the images clearly show the corresponding magnetic flux states in the grain boundary junction. The spatial modulation of the Josephson current density by the external magnetic field is imaged directly with a spatial resolution of about 1 micrometer.

Grain boundaries in the high temperature superconductors are known to act as weak links limiting the transport-critical current density of polycrystalline materials (*1*). Whereas the weak links of grain boundaries are certainly disappointing with respect to high current applications of the cuprate superconductors, the same weak link behavior of grain boundaries can be used for the fabrication of reliable Josephson elements required for microelectronics applications. Recently, artificially generated, "engineered" grain boundary Josephson junctions (GBJs) have been fabricated in a controllable and reproducible way by different techniques [for a recent review see (*2*)] and shown to be useful for numerous applications. However, despite considerable recent research effort, the physics of GBJs in the high temperature superconductors is not completely understood.

Weakly coupled superconductors such as grain boundary junctions show phase coherence phenomena on macroscopic length scales (*3*, *4*). For example, magnetic flux penetrating the grain boundary results in a spatial variation of the phase difference between the grains. This difference, in turn, causes a spatial modulation of the supercurrent density across the grain boundary. In typical electrical transport experiments, only the spatially integrated quantities such as the critical current I_c and its dependence on an applied magnetic field B are measured. For a spatially homogeneous Josephson junction with spatial dimensions that are small compared to the Josephson penetration depth λ_J, the $I_c(B)$ dependence follows the well-known Fraunhofer diffraction pattern (*3*). The integral transport properties of GBJs suggest that they are almost ideal overdamped Josephson junctions (*2*). Unfortunately, the interpretation of the integral quantities is often ambiguous. A more crucial test for the Josephson nature of grain boundaries would be the direct measurement of the spatial variation of the phase difference due to magnetic flux penetrating the grain boundary. We have used low temperature scanning electron microscopy (LTSEM) (*5–7*) to image directly the Josephson current density of $YBa_2Cu_3O_{7-\delta}$ GBJs with a spatial resolution of about 1 μm. Our experiments clearly show the spatial oscillation of the Josephson current density in the presence of an applied magnetic field. In particular, regions where the supercurrent flows in the same or opposite direction of the applied bias current are seen. When the applied magnetic field was varied, different magnetic flux states with up to 10 Josephson vortices could be imaged. Here, by Josephson vortex we mean a complete oscillation of the Josephson current density corresponding to a shift of the phase difference of 2π (*3*).

The GBJs used in our experiments were fabricated by depositing epitaxial, *c* axis–oriented $YBa_2Cu_3O_{7-\delta}$ films on symmetrical [001] tilt $SrTiO_3$ bicrystal substrates by pulsed laser deposition. The bicrystal substrate consists of two single crystals that were fused together with a misorientation angle of 24°. The thickness *d* of the film was about 300 nm. The GBJs are obtained by the patterning of narrow lines of width *W* ranging between 2 and 50 μm across the grain boundary, with the use of electron beam lithography and argon ion beam etching (*8*). For the LTSEM measurements, the sample was mounted onto a temperature-controlled cooling stage (*9*) in such a way that the surface of the sample could be scanned directly by the focused electron beam of a scanning electron microscope. Small magnetic fields on the order of a few microTeslas applied parallel to the grain boundary are generated by a normal conducting coil. A sketch of the experimental setup is shown schematically in Fig. 1. During the scanning process, the GBJ was biased at a constant current I_b slightly above the critical current I_c, and the electron beam–induced change $\delta V(x_0, y_0)$ of the GBJ voltage V was recorded as a function of the beam coordinates (x_0, y_0). A pulsed electron beam (energy = 15 keV, beam current = 10 to 100 pA, repetition rate = 20 kHz) was used, and $\delta V(x_0, y_0)$ was detected by a lock-in technique. The effect of electron beam irradiation can be considered as a local heating effect resulting in an increase (δT_0) of the local sample temperature at the position of the beam focus. The diameter of the perturbed area, which determines the spatial resolution, is about 1 μm. In our experiments the beam power was kept small (≤0.5 μW) so that the electron beam could be considered as an almost passive probe.

The GBJ can be treated as a quasi–one-dimensional Josephson junction, because the film thickness of about 300 nm is less than the Josephson penetration depth λ_J of the GBJ (*3*). We consider a quasi–one-dimensional Josephson junction extending in the *y* direction with a sinusoidal current-phase relation $J_s(y) = J_c(y)\cdot\sin\varphi(y)$. That is, the supercurrent density J_s is given by the product of the maximum Josephson current density J_c and the sine of the phase difference φ between the superconducting electrodes. For the case of a narrow junction ($W \leq \lambda_J$), shielding effects can be neglected and the junction is penetrated homogeneously by an external magnetic field applied in the *z* direction. The external magnetic field causes a linear increase of the phase difference $\varphi(y) = qy$ along the junction, where

$$q = \frac{2\pi d_m}{\Phi_0} B$$

Here d_m denotes the effective magnetic thickness of the junction and Φ_0 represents

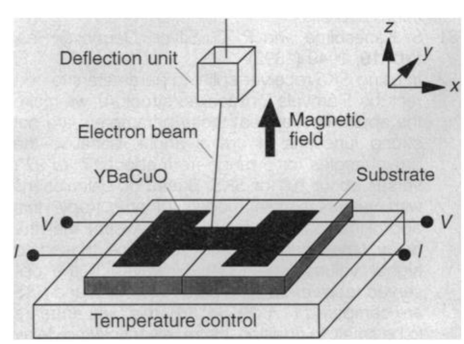

Fig. 1. Sketch of the sample configuration and the LTSEM setup.

G. M. Fischer, B. Mayer, R. Gross, T. Nissel, K.-D. Husemann, R. P. Huebener, Physikalisches Institut, Lehrstuhl Experimentalphysik II, Universität Tübingen, Morgenstelle 14, D-72076 Tübingen, Germany.
T. Freltoft, Y. Shen, P. Vase, NKT Research Center, DK-2605 Brøndby, Denmark.

*Present address: Physics Department, The Technical University of Denmark, DK-2800 Lyngby, Denmark.

the magnetic flux quantum. Hence, for an ideal junction with a constant $J_c(y)$, the supercurrent density is sinusoidally modulated [$J_s(y) \propto \sin(qy)$] along the junction. The spatial variation of the phase difference and the supercurrent density of such an ideal Josephson junction are shown in Fig. 2, A and B, respectively. The magnetic flux penetrating the junction along the extension of a complete oscillation of the Josephson current, called a Josephson vortex, is one magnetic flux quantum. We schematically sketched the location of the corresponding Josephson vortices (Fig. 2C). For larger Josephson junctions, self-field effects due to the current flowing through the junction can no longer be neglected. These effects result in a nonlinear increase of the phase difference along the junction and consequently in a more complex, nonsinusoidal modulation of the supercurrent density (3, 4).

In the case of small electron beam perturbation, the electron beam–induced change of the junction voltage can be expressed as

$$\delta V(y_0) \propto \frac{\partial V}{\partial I}|I = I_b \delta I_s(y_0)$$

where the electron beam–induced change of the supercurrent $\delta I_s(y_0)$ is the sum of a local [$\delta I_s^l(y_0)$] and a nonlocal [$\delta I_s^{\varphi}(y_0)$] signal contribution (10, 11). For narrow Josephson junctions ($W \leq \lambda_J$), the nonlocal signal contribution usually can be neglected. The same is true for wide Josephson junctions, if the electron beam perturbation is small and if the applied magnetic field corresponds to that of a maximum of the $I_c(B)$ dependence. These conditions apply for most of our experiments. A good approximation of the local signal contribution is given by $\delta I_s^l(y_0) \propto \sin\varphi(y_0)$ (10). That is, the electron beam–induced voltage change is proportional to the Josephson current density at the beam position. Scanning the current-biased GBJ and measuring $\delta V(y_0)$ as a function of the beam coordinates, we obtain a voltage image showing the distribution of the Josephson current density.

A typical LTSEM voltage image of the Josephson current-density distribution in a 23-μm-wide $YBa_2Cu_3O_{7-\delta}$ GBJ recorded at $T = 83$ K is shown in Fig. 3. The applied magnetic field corresponds to the fifth local maximum of the $I_c(B)$ dependence. For the measurement, the junction was biased close to the critical current at $I_b = 0.8$ mA, resulting in a junction voltage of 3 μV. In Fig. 3A, bright and dark regions correspond, respectively, to $\delta V > 0$ and $\delta V < 0$, with maximum voltage signals of about 30 and −15 nV. That is, in the bright and dark regions the local supercurrent and the applied bias current are parallel and antiparallel, respectively. The LTSEM signals are restricted to a strip about 1 μm wide along the grain boundary. This width is determined by the finite spatial resolution of the LTSEM technique (~1 μm). No voltage signal was detected either by scanning of the superconducting electrodes on both sides of the grain boundary or by scanning of the substrate adjoining the superconducting film. Furthermore, for bias currents less than the critical current, the voltage response of the GBJ disappears. To compare the LTSEM measurement directly to the behavior of a spatially homogeneous, narrow Josephson junction (Fig. 2), a single line scan along the grain boundary is plotted in Fig. 3B. In this representation, the voltage signal is plotted vertically during the horizontal scan. The spatial modulation of the critical current density is clearly visible. Deviations from the ideal sinusoidal oscillation shown in Fig. 2B are caused by spatial inhomogeneities of the maximum Josephson current density of the GBJ and by the fact that the measured sample is not small ($W/\lambda_J \approx 20$).

The LTSEM images of a series of successive vortex states recorded for an increasing applied magnetic field at $T = 86.5$ K are shown in Fig. 4. The images were obtained with a 10-μm-wide $YBa_2Cu_3O_{7-\delta}$ GBJ ($W/\lambda_J \approx 10$). Again, bright and dark regions correspond to sample regions yielding positive and negative voltage signals, respectively. Fig. 3A shows the voltage image for the zero vortex state obtained for the zero-applied magnetic field. Along the whole junction, only positive voltage signals are detected. The spatially inhomogeneous signal is mainly caused by a spatially inhomogeneous maximum Josephson current density and by nonlocal signal contributions. These contributions are obtained if the junction is not biased exactly at the absolute maximum of the $I_c(B)$ dependence. In Fig. 3, B to G, the applied magnetic fields correspond to the 1–2, 2–3, . . . 6–7 vortex states, respectively. In the experiment, one vortex after the other could be introduced into the sample by increasing the magnetic field. As expected theoretically, the spacing between the vortices becomes smaller for the higher vortex states, and the position of the vortex changes from each state to the other. The small deviations from a perfectly symmetrical signal

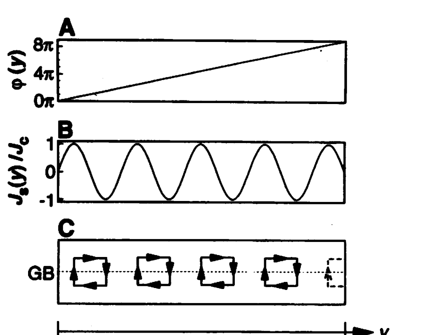

Fig. 2. Variation of (**A**) the phase difference $\varphi(y_0)$ and (**B**) the normalized supercurrent density $J_s(y_0)/J_c$ along an ideal narrow Josephson junction. The location of the Josephson vortices is schematically sketched in (**C**) (GB, grain boundary).

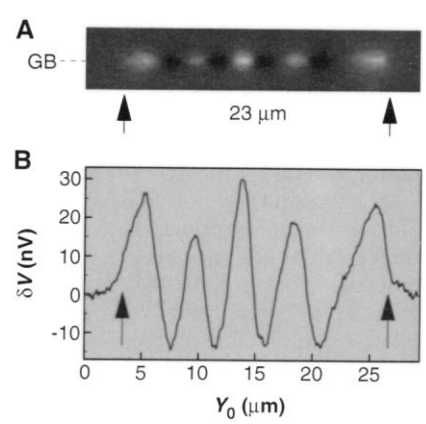

Fig. 3. (**A**) LTSEM voltage image of the 4–5 vortex state in a 23-μm-wide $YBa_2Cu_3O_{7-\delta}$ GBJ at $T = 83$ K. The edges of the GBJ are indicated by the arrows. The position of the grain boundary is marked by the broken line. Bright and dark regions correspond to sample regions yielding a positive and negative voltage signal, respectively. (**B**) Single line scan along the grain boundary with the voltage signal plotted vertically during the horizontal scan.

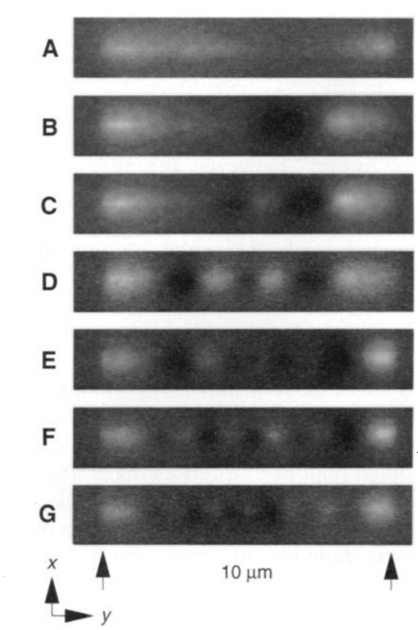

Fig. 4. LTSEM voltage images of a series of vortex states in a 10-μm-wide $YBa_2Cu_3O_{7-\delta}$ GBJ recorded at $T = 86.5$ K. The applied magnetic fields correspond to the 0, 1–2, 2–3, . . . 6–7 vortex states in (**A** to **G**), respectively. Bright and dark regions correspond to sample regions yielding a positive and negative voltage signal, respectively.

distribution again are caused by the nonlocal effect.

We have directly imaged static magnetic flux states in high temperature GBJs. Our experiments clearly show that the behavior of the high critical temperature junctions is close to that expected for ideal Josephson junctions. In particular, the maximum Josephson current density is quite homogeneous on a micrometer scale, and there are well-defined static magnetic flux states in the presence of an applied magnetic field.

REFERENCES AND NOTES

1. P. Chaudhari *et al., Phys. Rev. Lett.* **60**, 1653 (1988).
2. R. Gross, in *Interfaces in Superconducting Systems*, S. L. Shinde and D. Rudman, Eds. (Springer, New York, 1992), chap. 6.
3. A. Barone and G. Paterno, *Physics and Applications of the Josephson Effect* (Wiley, New York, 1982).
4. K. K. Likharev, *Dynamics of the Josephson Junctions and Circuits* (Gordon & Breach, Philadelphia, 1986).
5. R. P. Huebener, *Adv. Electron. Electron Phys.* **70**, 1 (1988).
6. R. Gross *et al., IEEE Trans. Magn.* **25**, 2250 (1989); *Z. Phys. B* **75**, 423 (1989); *Physica B* **169**, 415 (1991); *Appl. Phys. Lett.* **62**, 2871 (1993).
7. J. Mannhart *et al., Science* **245**, 839 (1989).
8. P. Vase, Y. Q. Shen, T. Freltoft, *Appl. Surf. Sci.* **46**, 61 (1992).
9. R. Gross, J. Bosch, H.-G. Wener, J. Fischer, R. P. Huebener, *Cryogenics* **29**, 716 (1988).
10. J. Bosch, R. Gross, M. Koyanagi, R. P. Huebener, *J. Low Temp. Phys.* **68**, 245 (1987); see also *Phys. Rev. Lett.* **54**, 1448 (1985).
11. J. J. Chang, C. H. Ho, D. J. Scalapino, *Phys. Rev. B* **31**, 5826 (1985).

12. Supported by the European Community ESPRIT Basic Research Project 7100 and the Bundesminister für Forschung und Technologie (project no. 13N5843).

18 October 1993; accepted 7 December 1993

Making Ceramics "Ductile"

Brian R. Lawn,* Nitin P. Padture,† Hongda Cai,† Fernando Guiberteau‡

Distributed irreversible deformation in otherwise brittle ceramics (specifically, in silicon carbide and micaceous glass-ceramic) has been observed in Hertzian contacts. The deformation takes the form of an expanding microcrack damage zone below the contact circle, in place of the usual single propagating macrocrack (the Hertzian "cone fracture") outside. An important manifestation of this deformation is an effective "ductility" in the indentation stress-strain response. Control of the associated brittle-ductile transition is readily effected by appropriate design of weak interfaces, large and elongate grains, and high internal stresses in the ceramic microstructure.

Ceramics have been cited as the "materials of the future." However, ceramics are also notoriously brittle and are subject to catastrophic failure from the growth of a single dominant crack (*1*). They are limited in their use as load-bearing materials by a low intrinsic toughness and, correspondingly, a lack of ductility to absorb mechanical energy. Of the various mechanisms that have been advocated for imparting toughness to ceramics (*1*), the most widespread and practical is that of "bridging," in which frictional pullout of interlocking grains and second-phase particles retards crack-wall separation (*2, 3*). Toughness then becomes a rising function of crack size [so-called toughness-curve, or resistance-curve, behavior (*1*)]. A most important element in the enhancement of bridging is the controlled introduction of weak interfaces on the microstructural scale, to deflect the primary crack and thereby generate a more effective interlocking structure. One can also enhance bridging by coarsening and elongating the grain structure and by incorporating internal mismatch stresses (*1, 4, 5*). Thus to gain toughness in ceramics, one builds in microstructural heterogeneity. However, there is a price to pay. Toughness is improved, but only in the "long-crack" region. In the "short-crack" region, built-in weakness can enhance fracture at the microstructural level, reducing laboratory strength (6) and increasing the susceptibility to wear and erosion (*7, 8*).

In view of this tendency toward countervailing interrelations in toughness properties, surprisingly little effort has been made to understand the seemingly deleterious short-crack properties of heterogeneous ceramics. We argue that these same seemingly deleterious properties also have potential benefits. The impetus for this assertion comes from our recent contact study on a moderately tough, coarse-grain alumina (*9*). Our test uses the classical Hertzian configuration of an indenting sphere on a flat specimen surface (*10*). A rich literature exists for Hertzian tests on homogeneous brittle solids, notably glass, in which a cone-shaped crack (the Hertzian fracture) forms in a region of weak surface tensile stress outside the contact circle (*11–16*). No such literature exists for analogous tests on heterogeneous tough ceramics. In our study on coarse alumina, we found no well-defined cone crack but rather a damage zone of distributed intergranular microfractures in a region of high shear stress below the contact circle. Stress-induced intragrain twins appeared to act as essential crack precursors in the alumina by concentrating stresses at the weak grain boundaries. The subsurface microfracture damage zone expanded with repeat loading, indicating a pronounced "fatigue" characteristic.

We have performed Hertzian tests on ceramic systems whose microstructural heterogeneity was tailored by heat treatments. In their base homogeneous forms, these ceramics are classically brittle and exhibit the familiar cone fractures. In their heterogeneous forms, however, these same ceramics are subject instead to subsurface microfracture, leading to an effective "ductile" response in the contact behavior. The results have profound implications concerning the capacity of brittle solids to sustain mechanical damage and absorb energy. Most important, the results suggest ways in which such radical "brittle-ductile transitions" in the mechanical response of ceramics may be effected by controlled microstructural modifications.

In our Hertzian test, a hard sphere of radius r was loaded onto a flat specimen surface. From the load P and contact radius a, we plot indentation stress $p_0 = P/\pi a^2$ versus indentation strain a/r (*17*) to produce an indentation stress-strain curve. A special specimen configuration, consisting

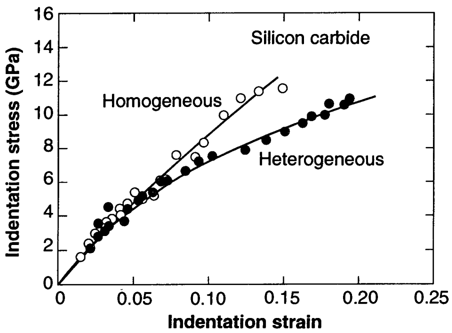

Fig. 1. Indentation stress-strain curve for silicon carbide in homogeneous fine-grain and heterogeneous coarse-grain forms. Data taken with tungsten carbide spheres in the radius range r from 1.58 to 12.7 mm.

Materials Science and Engineering Laboratory, National Institute of Standards and Technology, Gaithersburg, MD 20899, USA.

*To whom correspondence should be addressed.
†Guest scientist from the Department of Materials Science and Engineering, Lehigh University, Bethlehem, PA 18015, USA.
‡Guest scientist from the Departamento de Física, Universidad de Extremadura, 06071—Badajoz, Spain.